Biomechanical characterization of the passive mechanical response of the thoracic aorta in chronic hypoxic newborn lambs using a evolutionary strategy

Eugenio Rivera[1‡*], Claudio Canales[1‡], Matías Pacheco[1], Claudio García-Herrera[1], Demetrio Macías[2], Diego J. Celentano[3], Emilio A. Herrera[4]

1 Departamento de Ingeniería Mecánica, Universidad de Santiago de Chile, Santiago, Chile
2 ICD, P2MN, L2n, Université de Technologie de Troyes, ERL 7004, CNRS, Troyes, France
3 Departamento de Ingeniería Mecánica y Metalúrgica, Pontificia Universidad Católica de Chile, Santiago, Chile
4 Laboratorio de Función y Reactividad Vascular, Programa de Fisiopatología, ICBM, Universidad de Chile, Santiago, Chile

‡These authors share first authorship on this work.
* eugenio.rivera@usach.cl

Abstract

The present study involves experiments and modelling aimed at characterizing the passive structural mechanical behavior of the chronic hypoxic lamb thoracic aorta, whose gestation, birth and postnatal period were carried at high altitude (3,600 masl). To this end, the mechanical response was studied via tensile, ring opening and pressurization tests. The tensile and pressurization tests measurements were used simultaneously to calibrate the material parameters of the Gasser-Holzapfel-Ogden (GHO) anisotropic constitutive model through an analytical-numerical optimization procedure solved with an evolutionary strategy that guarantees a stable response of the model. The model and procedure of calibration adequately adjust to the material behavior in a wide deformation range with an appropriate physical description. The ring opening test was used in order to assess the influence of the residual stresses on the predicted material response in the pressurization test.

The results of this study predict the mechanical response of the lamb thoracic aorta under generalized loading states like those that can occur in physiological conditions and/or in systemic arterial hypertension. Finally, the novel use of the evolutionary strategy, together with the set of experiments and tools used in this study, provide a robust alternative to validate biomechanical characterizations.

Keywords

Lamb aorta, Evolutionary strategy, Constitutive models, Biomechanical properties, Numerical simulation, Hypoxia.

Author summary

The mechanical response of the aorta artery is mainly due to its three-layer structure and the main microstructural components, which give the material a hyperelastic,

anisotropic, and rate-dependent character. Currently, there are a series of constitutive models that include some microstructural characteristics, that have been widely used in soft tissue studies. However, one of the main difficulties when using them is to determine reliable parameters that reflect the physical responses observed in the biomechanical tests. In this work we apply an evolutionary strategy for the calibration of material parameters of an anistropic constitutive model. The procedure includes the simultaneous adjustment of two tensile curves and a pressurization curve. Then, we computationally simulate the biomechanical tests to validate the parameters obtained and quantify the effects of residual stresses within an arterial wall. The use of an evolutionary strategy was convenient in the characterization, since it showed excellent results in the adjustment of non-linear mechanical responses with multiple restrictions.

Introduction

Pregnancy and birth under hypobaric hypoxia as seen in high-altitude populations increase fetal and neonatal complications [1, 2]. The most common cardiovascular complications are pulmonary arterial hypertension of the newborns (PAHN) and right ventricular remodelling. These conditions are associated with physiological changes and structural alterations of the blood vessels such as an increased reactivity and remodeling [3–6], involving geometric changes in the structure of the arterial walls [4, 7–9].

During the last years, several studies highlighted the potential benefits of postnatal treatment with melatonin to cope PAHN, showing that it has effective antioxidant, vasodilator, antiremodeling and antihipertensive effects at the pulmonary level [3, 5, 6, 9, 10]. Although melatonin decreased large arteries thicknesses, such as the main pulmonary and aorta arteries, no biomechanical changes has been observed [2]. However, few is known still about the biomechanical changes that take place on the major arteries of the circulatory system due to melatonin administration [2].

In this context, there is great interest in evaluating the mechanical response of the arteries of animals affected by PAHN [3], since this biomechanical knowledge becomes an essential information for the development of proper diagnostics and treatment in cardiovascular and cardiopulmonary impairments [11, 12].

An important aspect that must be developed in biomechanical studies is the mechanical characterization of biological tissues, where it is necessary to choose a constitutive model able to properly define specific characteristics between materials [13]. A passive behavior analysis usually considers an elastic rate-independent material response, under the assumption of incompressibility [14, 15]. While several authors have characterized the arterial response using isotropic models which do not consider the structure of the arterial wall [16–19], others have incorporated some microstructural characteristics (i.e., stiff structure provided by the collagen fibers) present in the blood vessels motivated by the intrinsic anisotropic response [15, 20]. The formulations of the constitutive models were developed within the framework of the mechanics of the nonlinear continuum, and then implemented in the context of the finite element method (FEM) [20–22].

In order to characterize a hyperelastic material it is necessary to fit the experimental data from different mechanical tests to an hyperelastic constitutive model. The association between the experimental data and the mathematical model is done through an objective function that needs optimization. It is noteworthy to mention that several methods have been employed to characterize the constitutive parameters of a hyperelastic material [45–47]. Moreover, different authors have used the Least-Squares regression method, which is based on an iterative algorithm that requires the definition of an initial condition and the differentiation of an objective function. Another method

widely used is the Levenberg-Marquardt Method (LMM); however, it only performs a local search for the optimum and its convergence is highly dependent on the initial condition [49]. To find the parameters of an anisotropic hyperelastic model, another option is the use a meta-heuristic optimization technique that belongs to the set of evolutionary strategies (ES) [23]. The main reason for this choice is that ES useful in solving inverse problems, such as retrieving the constitutive parameters of a model, in different scientific domains [24–26]. Furthermore, in contrast to Gradient Descent methods, ES are not local optimisation techniques and they are less sensitive to initialisation [50]. Also, ES do not require knowledge of any initial condition or the gradients of a function [51]. In addition, there is not need to compute complicated derivatives nor to define restrictions when aplying ES [52]. The only requirement is to define the search space and an objective or fitness functional involving the parameters to be retrieved. In summary, ES seem well suited for the characterization of non-linear materials with multiple constraints.

The objective of the present work is to characterize the passive mechanical properties of the aorta artery of lambs gestated and born under chronic hypoxia at high altitude (3,600 masl) suffering from PAHN. To that end, we have structured this contribution as follows. We firstly describe the materials (lamb thoracic aorta) for two experimental groups, control and melatonin-treated. To assess biomechanical characteristics, we applied tensile, ring opening and pressurization tests in aortas. We also present the anisotropic constitutive model used for the mechanical characterization whose set of parameters was calibrated simultaneously from the tensile and pressurization tests measurements using an evolutionary strategy which is an algorithm orientated to global optimization. Finally, we describe the geometry, the boundary conditions, and the computational simulation of the pressurization test that includes the physiological measurements of axial stretch test and residual stresses derived from the ring closure process.

Materials and methods

0.1 Material

The tissue studied in this work by means of a pressurization test correspond to thoracic aortas (TA) of 7 newborns lambs gestated at high altitude (Putre, Chile, 3,600 masl). In this altitude level, the animals develop PAHN due to their gestation and birth under chronic hypobaric hypoxia [2, 3, 5, 6].

The lambs were randomly assigned to one of the two experimental groups, one control and other melatonin-treated. In the control group (CN, $n = 5$), lambs were administered with the vehicle orally (1.4% ethanol 0.5 ml kg^{-1} per day). In the melatonin group (MN, $n = 4$), lambs received oral melatonin (melatonin 1 mg kg^{-1} in ethanol 1.4%, 0.5 ml kg^{-1} per day, during 21 days, at dusk (20:00 h) to follow the circadian rhythm of melatonin). The dose of melatonin administered is sufficient to increase the plasma level approximately nine times without affecting the diurnal plasma concentration of this hormone [6, 10].

Animal care, maintenance and procedures were approved by the Bioethics Committee of the Faculty of Medicine of the Universidad de Chile (CBA # 0761 FMUCH) and were carried out according to the International Regulations for the Care and Use of Laboratory Animals published by the National Institutes of Health of The Unites States (Publication NIH No. 85-23, revised in 1996).

0.2 Biomechanical tests

0.2.1 Tensile test

The uniaxial tensile test applied on soft tissues is commonly used for characterizing the physical properties of the artery wall [15, 19, 27]. It constitutes a simple and easy to implement *in vitro* procedure to obtain the mechanical properties of tissues. However, it is insufficient to achieve a robust mechanical characterization, since it does not allow to replicate the complex loading conditions present in a physiological state [44]. Its main result is the stress-stretch relation under uniform deformation and it provides a set of parameters that have been used to compare the mechanical responses on soft tisues [2, 15, 29, 30].

It is important to highlight that the experimental results reported by Rivera et al. [2] were used in this work in the characterization procedures of the thoracic aorta artery. In the aforementioned work, the samples were analyzed immersed in calcium-free saline (Krebs), at 39^oC. The stress-stretch relationship was obtained by calculating the Cauchy axial stress as $\sigma = \frac{F}{A}$ where F is the axial load and A is the instantaneous cross sectional area (where the incompressibility condition is considered) and the axial stretching as $\lambda = \frac{L}{L_0}$ where L and L_0 are the instantaneous and initial measurements of the sample, respectively [2, 15].

Some biomechanical parameters of interest that allow comparing the tensile mechanical behavior in the physiological function range are the distensibility and the incremental module [11]. The distensibility is given by:

$$DC = \frac{D_s^2 - D_d^2}{D_s^2(P_s - P_d)} \tag{1}$$

where D_d and D_s are the diameters in diastole and sistole, respectively, while P_d and P_s are the pressures in diastole and sistole, which for the lamb model correspond to 60 and 120 mmHg, respectively [2, 31].

The incremental module represents the secant of the stress-stretch curve in the physiological pressure values (systolic and diastolic) and is given by:

$$E_{inc} = \frac{3}{DC}\frac{4t + D_s}{4t} \tag{2}$$

where t is average initial unloaded arterial wall thickness [11].

Finally, as detailed below, the experimental uniaxial tensile test results are considered in this work to obtain the material parameters that determine the mechanical behavior of the studied arteries by means of an anisotropic constitutive model which is later used in turn to estimate the residual stresses inside the arterial wall via computational simulation.

0.2.2 Ring opening test

The estimation of the residual stresses in the blood vessels provides an important factor for a robust and more realistic characterization of the mechanical behavior [15]. In the present work, the ring opening test was used to that end. The test consists in cutting a ring-shaped arterial piece along the radial direction which, due to internal stresses usually present in the tissue, is opened until a stabilization is achieved [2]. The angle formed by the cut ends defines the opening angle, α, as can be seen in Figure 1. This angle and the ring initial geometry are used to determine, by means of numerical simulations, the distribution of the residual stress along the thickness of the arterial wall [30]. In this estimation, the uniformity of the stress field along the height of the ring is assumed, as it is done by [15].

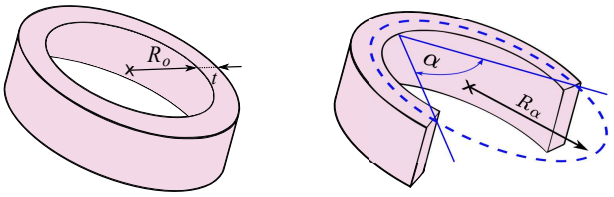

(a) (b)

Fig 1. Representation of the opening the rings process. (a) Initial and (b) Open configurations. R and t respectively denote the radius and thickness, α represents the opening angle.

0.2.3 Pressurization test

This test is intended to replicate the *in vivo* load of a blood vessel. In this test, a portion of a blood vessel is subjected to an axial stretch in the tensile machine followed by the application of internal pressure by means of a fluid (calcium-free saline) that is run through to the inside of the vessel to enact radial loading [27, 28, 32, 33]. For this purpose, the ends of the cylindrical samples of the thoracic aorta are fixed to metallic nozzles. The adopted set-up of the pressurization test is similar to that already described in [32]. Figure 2 shows the experimental assembly used in this work.

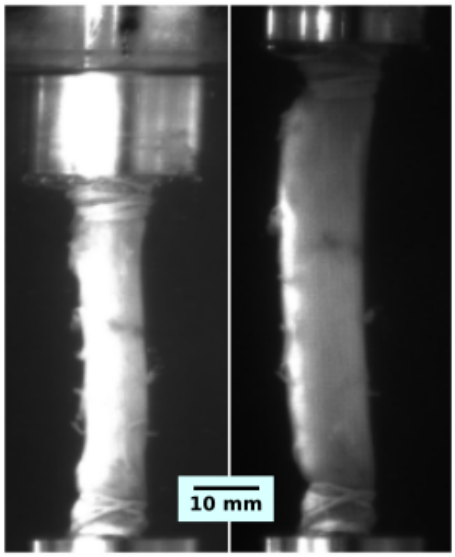

(a) (b)

Fig 2. Experimental assembly of the pressurization test. (a) Thoracic aorta without stretching and free of loads, immersed in Krebs; (b) Pressurization of a previously stretched thoracic aortic artery.

The axial stretch is calculated as $\lambda_z = \frac{L}{L_0}$ where L is the initial or physiological lengths and L_0 is the measurements after the artery was extracted. In this work, we used the value obtained from the first three sections of the thoracic aorta as reported by [2] which, for the control (CN) and melatonin (MN) group, has an average of $\lambda_z = 1.20$.

The internal pressure and external diameter of the vessel were obtained during the whole test using video recordings, which were then processed to plot the internal pressure vs. diametral stretch curve. The diametral stretch was defined as $\frac{D}{D_0}$, where D and D_0 denote the current and initial diameters of the vessel, respectively. In this

work, 10 successive loading cycles were run up to a pressure of 170 mmHg to precondition the samples. The last cycle was used to perform the inflation analysis.

0.3 Constitutive modelling

According to the measurements of the tensile tests, an elastic rate-independent material response was considered for the analyzed arteries. Furthermore, an incompressible arterial behavior was assumed due to the large amount of water present in them [14]. With the purpose of characterizing the mechanical response of the biological tissue, use is made of the constitutive hyperelastic model of Gasser-Holzapfel-Ogden (GHO) [22], whose deformation energy function W describes the behavior of the isothermal material under any load condition and can be defined in terms of the right Cauchy deformation tensor $\mathbf{C} = \mathbf{F}^T\mathbf{F}$, where $\mathbf{F}$ is the deformation gradient tensor and T is the transpose symbol. Using classical arguments of continuum mechanics, the Cauchy stress tensor is defined as $\sigma = 2J^{-1}\mathbf{F}\frac{\partial W}{\partial \mathbf{C}}\mathbf{F}$, where J is the determinant of $\mathbf{F}$.

The GHO model describes an anisotropic response of the arteries, since it includes the action of the collagen fibers that give the material a great resistance to traction. The functional form of the model is given by:

$$W = \frac{\mu}{2}(I_1 - 3) + \frac{k_1}{2k_2}\sum_{i=1,2}\left[\exp\left\{k_2[\kappa I_1 + (1-3\kappa)I_{4i} - 1]^2\right\} - 1\right] \quad (3)$$

where $I_1 = \mathbf{C} : \mathbf{I} = tr(\mathbf{C})$ is the first invariant of $\mathbf{C}$ and the invariants I_{4i}, with $i = 1, 2$, are defined as $I_{41} = \mathbf{C} : (a_1 \otimes a_1)$ y $I_{42} = \mathbf{C} : (a_2 \otimes a_2)$ such that a_1 and a_2 are two unit vectors defined in the reference configuration and arranged at a $\pm\gamma$ angle with respect to the axis of the vessel, which takes into account the orientations of two families of symmetric fibers. Furthermore, μ, k_1, k_2 and κ are material parameters (all of them with positive values). The parameter κ is associated with the dispersion of the fibers, taking values between 0 and 1/3 [22]. In Equation 3, the first term corresponds to a classical isotropic Neo-Hookean model, while the second and third terms have the objective of predicting the anisotropic behavior and the rigidization of the artery wall due to the action of the collagen fibers distributed symmetrically around the arterial wall, as illustrated in Figure 3. This model is aimed at characterizing consistently the anisotropy of the material present in the arterial tissues when they are subjected to moderate to high deformation levels. For simplicity, it must be kept in mind that specific responses of each arterial layer are not described by this model.

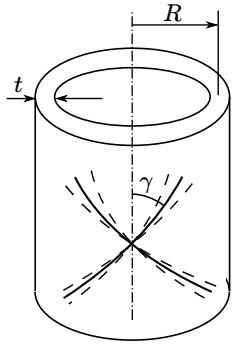

Fig 3. Representation of arterial wall with two embedded families of fibres. The mean orientations of the collagen fibres are characterized by the angle γ.

0.4 Numerical simulation

0.4.1 Closure of the ring

3D computational simulations were carried out of the ring closure process with the purpose of obtaining an estimation of the residual stresses along the thickness of the arterial wall. The reference (initial) configuration was assumed to be free of stresses and it corresponds to an open and stabilized ring, such that the described configuration was obtained based on the ring-opening tests reported by Rivera et al. [2]. The main experimental data required for the development of the simulations are summarized in Table 1, where a simplified geometry of the artery is assumed considering homogeneity and symmetry. The closure was performed establishing the boundary conditions used by García-Herrera et al. [15]. The ring closure was achieved by imposing displacements of the plane which defines the line AB and by restricting the movement of plane CD, as shown in the 2D scheme of Figure 4b.

Artery	R_0 $[mm]$	t_0 $[mm]$	α $[^\circ]$
TA CN	3.57±0.31	2.06±0.07	144±9
TA MN	3.26±0.15	2.14±0.07	140±16

Table 1. Geometric data to determine the initial and final configurations in the ring opening process, where R_0 is the internal radius, t_0 is thickness and alpha is opening angle. Values expressed as mean ± standard error of the mean (SEM) [2].

With the purpose of achieving the correct reconstruction of the closed geometry of a ring from an open geometry, an analytical equation was used to relate the mean radius of the open configuration with the mean radius of the closed configuration by means of the opening angle. The equation essentially relates the mean perimetric length of a closed artery with the mean arc length that is formed in the ring opening. The relation is defined by:

$$R_\alpha = \left(\frac{\pi}{\pi - \alpha}\right) R_m \tag{4}$$

where R_α is the mean radius of an open ring geometry, $R_m = R_0 + \frac{t}{2}$, is the mean radius of a closed ring geometry, and α is the opening angle (in radians), see Figure 1.

The 3D finite element mesh used in the numerical simulations was composed of 9,594 nodes which correspond to 8×25×40=8,000 hexahedral elements as shown in Figure 4a.

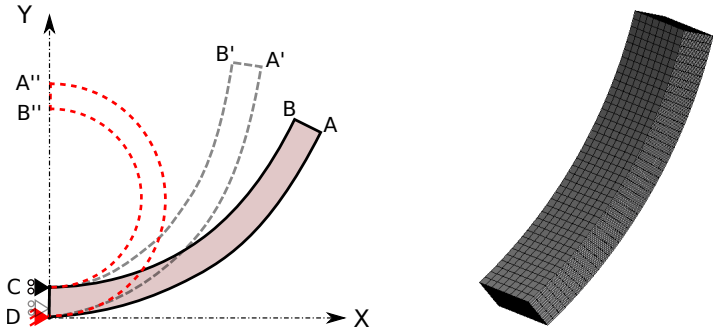

(a) (b)

Fig 4. (a) Representation 2D of the boundary conditions for the computational simulation of the closure of the rings. (b) View of the 3D finite element mesh.

0.4.2 Pressurization test

The pressurization test is an excellent complement to uniaxial tensile tests when characterizing and establishing parameters of a constitutive model. Additionally, the numerical simulation of this test allows evaluating the variation of the circumferential stresses at different levels of internal pressure, allowing to analyze extreme conditions and states of arterial hypertension.

In this work, the finite element analysis of this test corresponds to a 2D axisymmetric simulation, since the symmetries that come from assuming a perfectly cylindrical initial artery are considered. The simulation is made up of two fundamental steps. The first step is an axial stretch of the artery to its physiological length. The physiological elongation corresponds to a value of $\lambda_z = 1.20$, which is kept constant during the simulation of the pressurization stage. The second step is the pressurization process (inflation), where an internal pressure is applied to the arterial wall that covers the physiological range and extends to hypertension values, up to 170 mmHg. Figure 5-a summarizes this loading procedure.

The computational reconstruction corresponds to a rectangular surface (or longitudinal section) obtained by making a longitudinal cut to a cylindrical tube. The dimensions that define the geometry, i.e., the internal radius and thickness, were obtained from the average measurements of the thoracic aortic arteries obtained from ring opening tests. Meanwhile, the length was defined as the average of the samples obtained from the pressurization test. The dimensions corresponding to the internal radius, thickness and length of both groups were for CN: $R_0 = 3.57\ mm$, $t = 2.06\ mm$, $L = 14\ mm$ and for MN: $R_0 = 3.26\ mm$, $t = 2.14\ mm$, $L = 14\ mm$.

The mesh shown in Figure 5-b has 2626 nodes that correspond to $25 \times 100 = 2500$ elements (quadrilaterals). This mesh contains a refinement towards the base, where the artery is anchored, in order to properly capture the edge effects expected in this zone.

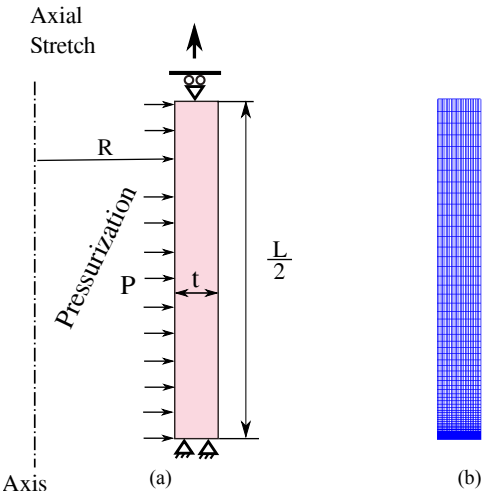

Fig 5. (a) Representation 2D of the boundary conditions for the computational simulation of the pressurization test. (b) View of the 2D finite element mesh.

0.5 Material parameters calibration procedure

0.5.1 Objective function

In order to model the arteries according to the GHO constitutive model [22], it is necessary to calibrate its parameters. For this purpose, different mechanical tests are

carried out on this material. Thus, it is necessary to propose a calibration procedure that maximizes, through the definition of an objective function, the similarity between the behavior of the hyperelastic model and the experimental data and also guarantees a stable response of such model.

By considering multiple mechanical tests in the characterization process, it is possible to capture the mechanical behavior of the arteries under different modes of deformation. Therefore, experimental measurements collected from the tensile (along both the longitudinal and circumferential directions) and pressurization tests are used in this work in order to obtain the material parameters of the GHO model.

Firstly, it should be noted that it is not possible to obtain a closed analytical expression of the Cauchy stress σ_1 for the GHO constitutive model when the material is subjected to uniaxial tensile stress. According to the procedure defined by Ogden [43], the mechanical response in this particular case can be determined by the following mathematical expressions:

$$\sigma_1(\mathbf{x}, \lambda_1, \lambda_2) = 2(\lambda_1^2 - \lambda_1^{-2}\lambda_2^{-2})W_1 + 2\lambda_1^2 \cos(\gamma - \beta)^2 W_4 + 2\lambda_1^2 \cos(\gamma + \beta)^2 W_6 \quad (5)$$

$$\sigma_2(\mathbf{x}, \lambda_1, \lambda_2) = 2(\lambda_2^2 - \lambda_1^{-2}\lambda_2^{-2})W_1 + 2\lambda_2^2 \sin(\gamma - \beta)^2 W_4 + 2\lambda_2^2 \sin(\gamma + \beta)^2 W_6 = 0 \quad (6)$$

where $W_i = \frac{\partial W}{\partial I_i}$ $(i = 1, 4, 6)$ and β denotes the sample orientation (i.e., $\beta = 0°$ and $90°$ for longitudinal and circumferential samples, respectively). It is possible to observe that σ_1 depends on λ_1 and λ_2 so, it is necessary to use equation 6, for a given set of parameters $\mathbf{x} = (\mu, \kappa, k_1, k_2, \gamma)$, in order to find the value of λ_2. This last operation is done through the Newton-Raphson method due to the nonlinear nature of the equation.

Secondly, the mechanical behavior of the pressurization test is modeled using the numerical approach presented in Section 0.4.2 since analytical expressions describing the material response in this test are only limited to certain conditions that are not met in this case [39]. To calculate the standardized quadratic errors of each of the mechanical tests, the following function can be defined:

$$J(\boldsymbol{y}, \hat{\boldsymbol{y}}) = \frac{1}{n} \sum_{i=1}^{n} \frac{(y_i - \hat{y}_i)^2}{|max(\boldsymbol{y}) - min(\boldsymbol{y})|} \quad (7)$$

where n is the number of experimental points, $\boldsymbol{y}$ are the experimental values and $\hat{\boldsymbol{y}}$ are the values predicted by the model. With this metric, it is possible to define the following objective function:

$$\min_{\mathbf{x} \in \mathbf{A}} f(\mathbf{x}) = J(\boldsymbol{\sigma}^{cir}, \hat{\boldsymbol{\sigma}}^{cir}) + J(\boldsymbol{\sigma}^{lon}, \hat{\boldsymbol{\sigma}}^{lon}) + 2J(\boldsymbol{\lambda}_\theta^{presu}, \hat{\boldsymbol{\lambda}}_\theta^{presu}) \quad (8)$$

where $\boldsymbol{\sigma}^{cir}$ and $\boldsymbol{\sigma}^{lon}$ are the uniaxial stress for the circumferencial and longitudinal tensile curves, respectively and $\boldsymbol{\lambda}_\theta^{presu}$ are the diametral stretches of the presurization test. It is worth mentioning that the cost of the pressurization curve is multiplied by 2, so that its weigth is equivalent to the cost of the uniaxial tests. This objective function is restricted to a stability domain given by the set $\mathbf{A}$ that is defined as:

$$\mathbf{A} = \left\{ \boldsymbol{x} \in \mathbb{R}^5 \mid \kappa \in]0, 1/3] \ \wedge \ \gamma \in [0, \frac{\pi}{2}] \ \wedge \ \frac{d\Psi}{d\lambda_1} - \frac{7\Psi}{5\lambda_1} < 0 \, \forall \, \lambda_1 \in \left\{ \lambda_i^{cir}, \lambda_i^{lon} \right\} \right\} \quad (9)$$

where $\Psi = W_1^{-1}[W_1 + \sin(\gamma + \beta)^2 W_4 + \sin(\gamma - \beta)^2 W_6]$. For more details about this stability criterion, please refer to Canales [34]. Lastly, the evolutionary strategies (ES) [35] are used to solve the nonlinear constrained optimization problem defined in equation 8 which serves as a link between the inversion method and the physics of the material that is being studied. The whole material parameters calibration procedure is summarized and illustrated in Figure 6.

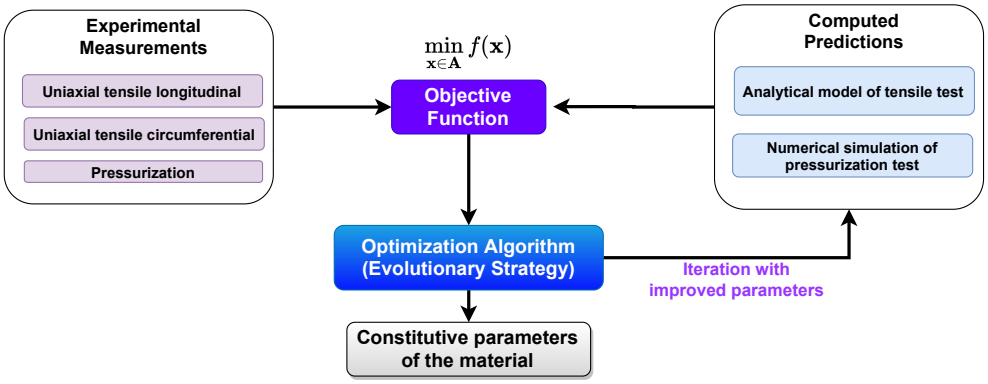

Fig 6. Algorithm of the inverse problem-solving method. The evolutionary loop shows the main steps of the optimization problem.

0.5.2 Evolutionary strategies

The optimization problem presented in equation 8 has a non-linear nature that is subjected to multiple constraints. ES have proven to be a suitable and a versatile tool to solve this kind of problems [38, 40] and, therefore, are used in this work. A brief description of them is presented below. (for a more details, we refer the interested reader to the excellent work of Macías et al. [41] or the book of Beyer [42].

The initial step before to the beginning of the optimization process is the random initialization of an assembly of vectors $\mathbf{x}$ that will constitute the initial population $P_\mu^{(g)}|_{g=0}$, where μ is the number of elements within the initial population and g is the generation of the population which is associated with the iteration of the algorithm. A canonical evolutionary optimization algorithm is based on the application, over a defined number of iterations, of two genetic operators with well defined roles. The first is the recombination, which exploits the search space through the exchange of information between ρ different elements of the population. The second operator is the mutation, which is used to explore the search space through the introduction of random variations in the population. The application of these genetic operators over the initial population leads to the generation of a secondary population $P_\lambda^{(g)}$ of λ elements. It is at this stage of the evolutionary loop that the link between the physics of the problem studied and the optimization algorithm is established. In the present work, this is done through the minimization of the functional defined by equation 8, which can also be interpreted as a measure of the similarity between the experimental data and the mechanical response of the hyperelastic constitutive model. Each element of the secondary population will be evaluated, and only those elements of $P_\lambda^{(g)}$ that minimize the objective function will be retained, through some selection scheme, as part of the population $P_\mu^{(g+1)}$ for the next iteration of the evolutionary loop. The procedure is repeated until a defined stopping criteria has been fulfilled. The respective sizes of the initial and the secondary populations, $P_\mu^{(g)}$ and $P_\lambda^{(g)}$, remain constant throughout the entire search process. In this work, the elitist selection (ES -$(\mu/\rho+\lambda)$) is used, which selects the junction of the initial and mutated populations. Consequently, a promising element belonging to the first initial population can survive throughout the entire optimization process. Although this attribute of the ES guarantees a monotonic decrement or increment of the fitness function, it can also make it prone to a premature convergence into a local optimum.

0.6 Statistic analysis

All the data were expressed as the *means* ± *standard error of the mean* (SEM), which is the ratio between the standard deviation and the square root of the number of specimens. The results were compared statistically by means of the non-parametric Mann-Whitney test for independent random samples. Significant differences were accepted when $p \leq 0.05$ (Prism 5.0; GraphPad).

Results and Discussion

0.7 Material characterization via tensile and pressurization tests

Figures 7 a and b present the graphs of the average stress-stretch curves of the thoracic aorta for the control (CN) and melatonin (MN) groups, respectively. Each figure contains the experimental data for the circumferential and longitudinal directions (the vertical bars indicate the standard error of the mean, SEM). It is seen that all the curves present a typical hyperelastic behavior, that is, a first linear stage followed by a transition stage, and finally a linear (rigidization stage).

Furthermore, as already mentioned, the experimental results of the tensile tests were used to determine material parameters of the anisotropic constitutive model of GHO described in Section 0.3. For simplicity, the material parameters were derived from each pair of average curves (longitudinal and circumferential) corresponding to each group, applying an evolution strategies (see Section 0.5.2). The analytical expressions of the stress field which assume flat stress conditions used to derive the material parameters, given explicitly in the paper by Garcia-Herrera et al. [15]. The values of the material parameters obtained are presented in Table 2. The curve corresponding to the fit is presented by means of the GHO constitutive model, using the values of the parameters and they provide physically motivated responses [36, 37] as can be seen in Figures 7 c and d. If we compare the parameters of the arterial groups (CN and MN), it is seen that the resultant values are similar and fit the experimental curves with sufficient precision, as shown by the values of the fitting quality for each curve (see Figures 7 a y b. The correlation indicator used was Efron's Pseudo R-Squared (r^2), which is shown in Table 2.

Artery	μ $[kPa]$	k_1 $[kPa]$	k_2	κ	$\gamma[^o]$	r^2_{circ}	r^2_{long}	$r^2_{without\ RS}$	$r^2_{with\ RS}$
TA CN	16.25	24.18	0.233	0.123	46.38	0.956	0.992	0.976	0.965
TA MN	16.58	27.97	0.757	0.253	49.23	0.994	0.959	0.996	0.988

Table 2. Material parameters of the GHO model for aorta artery and correlation indicators for tensile curves (r^2_{circ} and r^2_{long}), pressurization tests without and with residual stress ($r^2_{without\ RS}$ and $r^2_{with\ RS}$).

0.8 Estimation of residual stresses via the ring opening test

Using the nomenclature defined in Figure 1, Table 1 summarizes the geometric values basis of the opening test; these values are the internal radius R_0, the thitckness e_0 and the opening angle α, obtained by Rivera et al. [2].

We carried out 3D simulations of the ring openings with the purpose of obtaining an estimation of the residual stresses along the thickness of the arterial wall. These stresses not only make more robust the mechanical characterization of a given material [15], but they are also indicators of changes in the mechanical responses caused by pathologies; for example, in previous work the comparisons between arterial samples of healthy and

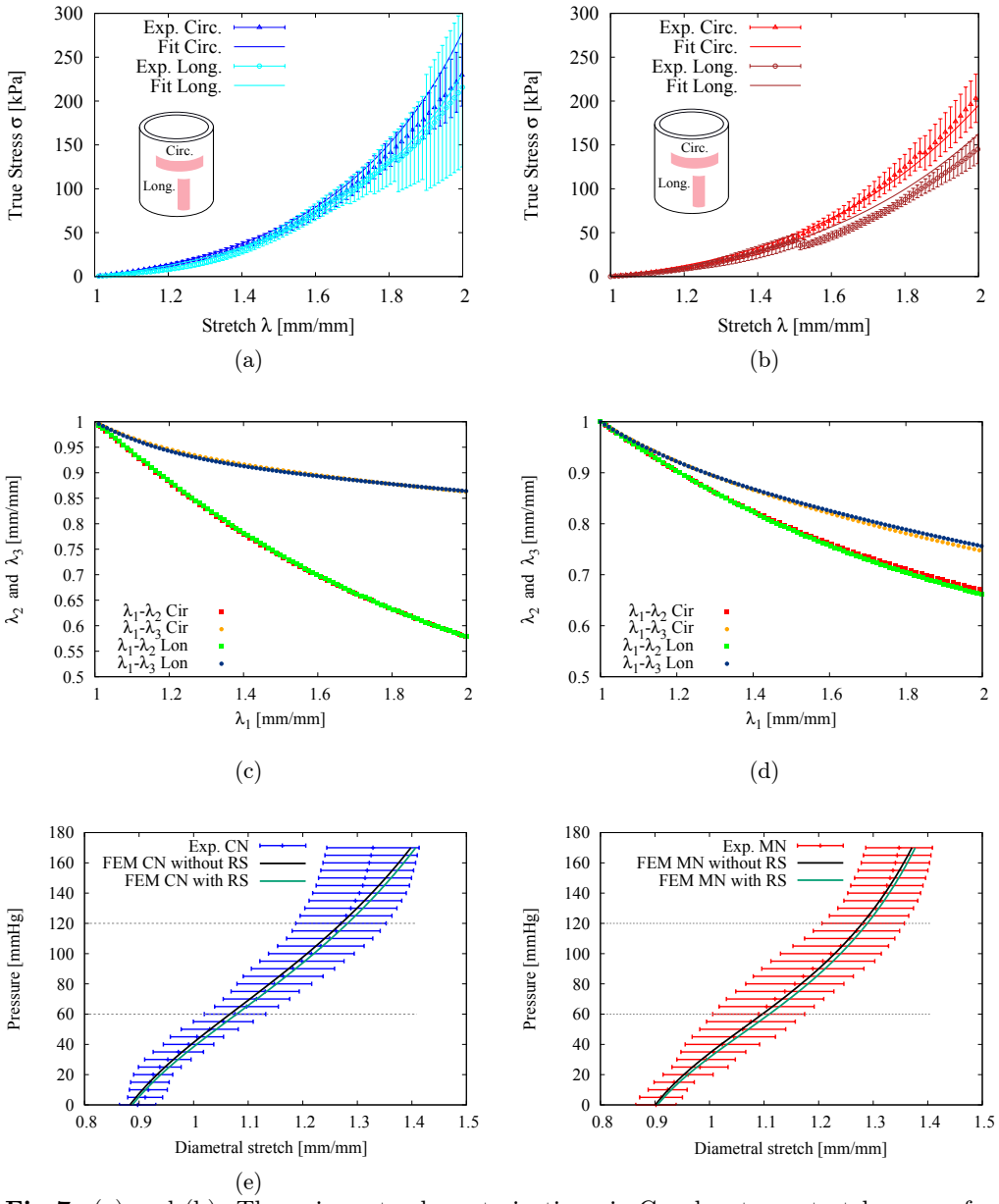

Fig 7. (a) and (b): Thoracic aorta characterization via Cauchy stress-stretch curves for control (CN) and melatonin (MN) group lambs. The fitting were compute via GHO's model. (c) and (d): Realistic numerical results of the GHO model tensile stretchs for the aorta artery. (e) and (f): FEM numerical simulation of the pressurization test and effects of the residual stress (RS) on the material response.

pathological groups (aneurysms and fetal growth restriction, among others), in human arteries [15] and of a model animal (Guinea pigs) [18, 30]. The reported results indicate, in general, that the residual stresses vary significantly between the healthy and the pathological groups.

The results of the numerical simulations obtained in the present work are summarized by means of the resulting circumferential residual stress obtained at the closing of the ring are presented in Table 5. The comparison between the CN and MN groups was made by means of circumferential stresses of the inner and outer faces ($\sigma_{\theta\ int}$ and $\sigma_{\theta\ out}$ respectively), its difference ($|\Delta\sigma| = |\sigma_{\theta\ int} - \sigma_{\theta\ out}|$) and its average ($\sigma_{mean} = (\sigma_{int} + \sigma_{out})/2$) [15, 30]. The values show a similar response between the CN and MN groups, not showing significant changes between the parameters associated with the residual stresses.

The analytical formula 4 used provides a good approximation of the average geometry of the arterial rings, the results of the main geometric data of the FEM simulation are presented in Table 3. The results obtained do not exceed 2% difference, compared to those reported by Rivera 2020 (see table 1).

Artery	R_0 $[mm]$	difference %	t_0 $[mm]$	difference %
SIM TA CN	3.50	1.96	2.059	0.04
SIM TA MN	3.23	0.92	2.126	0.65

Table 3. Geometrical results from the FEM simulation for the CN and MN group.

0.9 Assessment of the effect of residual stresses in the pressurization test

Figures 7 e and f shows pressure vs. diametral stretch curves corresponding to groups CN and MN for a value of axial stretch $\lambda_z = 1.20$. The experimental response of both groups is similar and there is no evidence of significant differences. The internal pressure curve vs. diametral stretch curves obtained with the GHO model via computational simulation FEM are also presented in mentioned figures. The horizontal lines denote the physiological range of diastole and systole of the cardiac cycle, which was estimated between 60 mmHg and 120 mmHg. The distensibility and incremental module measurements presented in Table 4 show similar biomechanical response in the physiological pressure range between the MN group and the CN group and no present significant changes. In the same table, by way of comparison, the values obtained by Rivera et al. [2] from the tensile tests are presented, it can be seen that these measurements show a similar biomechanical response.

Additionally, we present two cases of numerical simulations for pressurization, one that is without residual stresses and the other with residual stresses, in order to evaluate the effect of these stresses on the mechanical behavior. The results obtained show that the inclusion of residual stresses in our study does not have significant effects in the range of pressures considered (0-170 mmHg), with a slight shift of the curve to the right.

Also in the Table 5 is presented the circunferenctial stress for three different loading conditions (pressures 60, 120 and 170 mmHg). The comparison between the MM an CN groups in general do not present significant changes.

Conclusion

The experimental work, the modeling, and the numerical simulations based on the uniaxial tensile, ring-opening and pressurization tests on aorta artery samples have been

Thoracic Artery	Pressurization test results	
	$DC\ [mmHg^{-1}] \times 10^{-3}$	$E_{inc}\ [MPa]$
CN	5.53±0.47	0.241±0.029
MN	5.51±0.41	0.224±0.021
Thoracic Artery	Tensile test results	
	$DC\ [mmHg^{-1}] \times 10^{-3}$	$E_{inc}\ [MPa]$
CN (Rivera 2020)	4.63±0.36	0.249±0.022
MN (Rivera 2020)	4.65±0.43	0.220±0.024

Table 4. Distensibility, DC, and incremental modulus of elasticity, E_{inc}, obtained in the tensile by Rivera 2020 [2] and pressurization tests obtained in this work, with axial stretch $\lambda_z = 1.20$. Values were expressed as Mean ± SEM. Significant differences ($P \leq 0.05$): * vs. CN.

Thoracic Artery	Group	$\sigma_{\theta\ int}\ [kPa]$	$\sigma_{\theta\ out}\ [kPa]$	$\lvert\Delta\sigma_\theta\rvert\ [kPa]$	$\sigma_{\theta\ mean}\ [kPa]$
$P_i = 0$ mmHg	CN	-10.972	11.532	22.504	0.280
Residual stress (RS)	MN	-11.624	11.339	22.963	-0.143
$P_i = 60$ mmHg	CN	24.234	31.377	7.143	27.806
	MN	26.125	30.107	3.982	28.116
$P_i = 120$ mmHg	CN	130.63	66.929	63.701	98.780
	MN	157.14	57.763	99.377	107.45
$P_i = 170$ mmHg	CN	290.55	99.442	191.12	194.99
	MN	346.54	76.903	269.64	211.72

Table 5. Residual stress from the simulation of the ring closure of the arteries ($P_i = 0$). Circunferential stress from the simulation of the presurization on the thoracic aorta for pressures $P_i = 60,\ 120$ and 170 mmHg. The simulation added as initial values the residual stress and fisiological axial stretch $\lambda_z = 1.20$.

presented.

The main objective of this study was the biomechanical characterization of the aorta artery in lambs gestated and born at high altitude (3,600 masl), affected by pulmonary hypertension in newborns (PHN).

Experimental data from tensile tests and pressurization tests have been used to determine the material parameters of the Gasser-Holzapfel-Ogden constitutive model, where simultaneously the constitutive modelling the tensile (on two direction) and the pressurization test have been experimentally validated, obtaining high goodness of fit in curves. The evolutionary strategy procedure used ensures the stability of the constitutive model and as a consequence, physically motivated responses are obtained.

The addition of the residual stresses in the computer simulations of the pressurization test does not show important changes in the biomechanical behavior. However, it was observed that its inclusion favors the relaxation of the arterial wall.

Finally, the application of an evolutionary strategy to samples of an animal lamb model is an original contribution of this research.

Funding and acknowledgments

The work was funded by CONICYT-PCHA/Doctorado Nacional/2014-21140988 and projects FONDECYT 1170608 and 1151119..

References

1. Keyes L, Armaza F, Niermeyer S. et al. Intrauterine growth restriction, preeclampsia, and intrauterine mortality at high altitude in Bolivia. Pediatr Res. 2003 Jul;54: 20–25. https://doi.org/10.1203/01.PDR.0000069846.64389.DC

2. Rivera E, García-Herrera, C, González-Candia A, et al. Effects of melatonin on the passive mechanical response of arteries in chronic hypoxic newborn lambs. J Mech Behav Biomed Mater. 2020 Dec;112:104013. doi: 10.1016/j.jmbbm.2020.104013. PMID: 32846285.

3. Herrera EA, Pulgar VM , Riquelme RA, et al. High-altitude chronic hypoxia during gestation and after birth modifies cardiovascular responses in newborn sheep. Am J Physiol Regul Integr Comp Physiol. 2007 Jun;292(6):R2234–40. https://doi.org/10.1152/ajpregu.00909.2006

4. Papamatheakis DG, Blood AB, Kim JH and Wilson SM Antenatal hypoxia and pulmonary vascular function and remodeling. Curr Vasc Pharmacol. 2013 Sep; 11(5): 616–640. PMCID: PMC4527655

5. Herrera EA, Farías JG, Ebensperger G, et al. Pharmacological approaches in either intermittent or permanent hypoxia: A tale of two exposures. Pharmacol Res. 2015 Nov;101:94-101. doi: 10.1016/j.phrs.2015.07.011. PMID: 26215469.

6. Torres F, González-Candia A, Montt C, et al. Melatonin reduces oxidative stress and improves vascular function in pulmonary hypertensive newborn sheep. J Pineal Res. 2015 Apr;58(3):362-73. doi: 10.1111/jpi.12222. PMID: 25736256.

7. Gao Y, Raj JU. Hypoxic Pulmonary Hypertension of the Newborn. Compr Physiol. 2011 Jan;1(1):61-79. doi: 10.1002/cphy.c090015. PMID: 23737164.

8. Herrera EA, Ebensperger G, Krause, BJ, et al. Sildenafil reverses hypoxic pulmonary hypertension in highland and lowland newborn sheep. Pediatr Res. 2008 Feb;63(2):169-75. doi: 10.1203/PDR.0b013e31815ef71c. PMID: 18091352.

9. Astorga CR, González-Candia A, Figueroa EG, et al. Melatonin decreases pulmonary vascular remodeling and oxygen sensitivity in pulmonary hypertensive newborn lambs. Front Physiol. 2018 Mar 6;9:185. doi: 10.3389/fphys.2018.00185. PMID: 29559926; PMCID: PMC5845624.

10. Gonzaléz-Candia A, Candia AA, Figueroa EG, et al. Melatonin long-lasting beneficial effects on pulmonary vascular reactivity and redox balance in chronic hypoxic ovine neonates. J Pineal Res. 2020 Jan;68(1):e12613. doi: 10.1111/jpi.12613. PMID: 31583753.

11. Laurent S, Cockcroft J, Van Bortel, et al. Expert consensus document on arterial stiffness: methodological issues and clinical applications. Eur Heart J. 2006 Nov;27(21):2588-605. doi: 10.1093/eurheartj/ehl254. PMID: 17000623.

12. Dodson RB, Rozance PJ, Fleenor BS, et al. Increased stiffness and extracellular matrix reorganization in intrauterine growth restricted (IUGR) fetal sheep. Pediatr Res. 2013 Feb;73(2):147-54. doi: 10.1038/pr.2012.156. PMID: 23154756.

13. Marsden JE, Hughes TJR. Mathematical Foundations of Elasticity. Prentice-Hall; 1982. ISBN 0-13-561076-1.

14. van Oijen, Christiaan Hendrikus Gerardus Arnoldus. Mechanics and design of fiber-reinforced vascular prostheses. Technische Universiteit Eindhoiven. Ph.D. thesis; 2003. https://pure.tue.nl/ws/files/2458894/200311647.pdf

15. García-Herrera C, Bustos C. Celentano D, et al. Mechanical analysis of the ring opening test applied to human ascending aortas. Comput Methods Biomech Biomed Engin. 2016 Dec;19(16):1738-1748. doi: 10.1080/10255842.2016.1183125. PMID: 27178265.

16. Fung, Yuan Cheng. Biomechanics: Mechanical Properties of Living Tissues. Springer-Verlag; 1993. ISBN 0387979476.

17. Claes, Els. Mechanical study of human coronary arteries and their vascular grafts. Universidad Politécnica de Madrid. Ph.D. thesis; 2010. Spanish. https://oa.upm.es/3859/

18. Cañas D, Herrera EA, García-Herrera C, et al. Fetal Growth Restriction Induces Heterogeneous Effects on Vascular Biomechanical and Functional Properties in Guinea Pigs (Cavia porcellus). Front Physiol. 2017 Mar 10;8:144. doi: 10.3389/fphys.2017.00144. PMID: 28344561; PMCID: PMC5344887.

19. García-Herrera C, Celentano DJ, Cruchaga, MA, et al. Mechanical characterisation of the human thoracic descending aorta: experiments and modelling. Comput Methods Biomech Biomed Engin. 2012;15(2):185-93. doi: 10.1080/10255842.2010.520704 PMID: 21480018.

20. Holzapfel GA. Determination of material models for arterial walls from uniaxial extension tests and histological structure. J Theor Biol. 2006 Jan 21;238(2):290-302. doi: 10.1016/j.jtbi.2005.05.006. PMID: 16043190.

21. Peña E, Calvo B, Martínez MA, Doblaré M. An anisotropic visco-hyperelastic model for ligaments at finite strains. Formulation and computational aspects. International Journal of Solids and Structures Feb 2007;44(3):760-778. https://doi.org/10.1016/j.ijsolstr.2006.05.018

22. Gasser TC, Ogden RW, Holzapfel GA. Hyperelastic modelling of arterial layers with distributed collagen fibre orientations. J R Soc Interface. 2006 Feb 22;3(6):15-35. doi: 10.1098/rsif.2005.0073. PMID: 16849214; PMCID: PMC1618483

23. Michalewicz, Zbigniew. Genetic Algorithms + Data Structures = Evolution Programs (3rd Ed.). Springer-Verlag; 1996. ISBN 3540606769.

24. Djurišić AB, Elazar JM, Raki AD Simulated-annealing-based genetic algorithm for modeling the optical constants of solids. Appl Opt. 1997 Oct 1;36(28):7097-103. doi: 10.1364/ao.36.007097. PMID: 18264214.

25. Vial A, Grimault AS, Macías, D, et al. Improved analytical fit of gold dispersion: Application to the modeling of extinction spectra with a finite-difference time-domain method. Physical Review B 2005 Feb 23;71(8):085416 https://doi.org/10.1103/PhysRevB.71.085416

26. Macías D, Vial A, Luna A, et al. Characterization of natural photonic structures by means of optimization strategies. Proc. SPIE 9429, Bioinspiration, Biomimetics, and Bioreplication 2015, 94290X (26 March 2015) https://doi.org/10.1117/12.2083850

27. García-Herrera C, Atienza JM, Rojo FJ, et al. Mechanical behaviour and rupture of normal and pathological human ascending aortic wall. Med Biol Eng Comput. 2012 Jun;50(6):559-66. doi: 10.1007/s11517-012-0876-x. PMID: 22391945.

28. García-Herrera C, Celentano DJ, Cruchaga, MA. Bending and pressurisation test of the human aortic arch: experiments, modelling and simulation of a patient-specific case. Comput Methods Biomech Biomed Engin. 2013;16(8):830-9. doi: 10.1080/10255842.2011.641123. PMID: 22224674.

29. Guinea, GV, Atienza JM, Rojo FJ, et al. Factors influencing the mechanical behaviour ofhealthy human descending thoracic aorta. Physiol Meas. 2010 Dec;31(12):1553-65. doi: 10.1088/0967-3334/31/12/001. PMID: 20980717.

30. Cañas D, García-Herrera C, Herrera EA, et al. Mechanical characterization of arteries affected by fetal growth restriction in guinea pigs (Cavia porcellus). J Mech Behav Biomed Mater. 2018 Dec;88:92-101. doi: 10.1016/j.jmbbm.2018.08.010. PMID: 30142566.

31. Peers A, Mellor DJ, Wintour EM, et al. Blood pressure, heart rate, hormonal and other acute responses to rubber-ring castration and tail docking of lambs. N Z Vet J. 2002 Apr;50(2):56-62. doi: 10.1080/00480169.2002.36251. PMID: 16032211.

32. Guinea GV, Atienza JM, Elices M, et al. Factors influencing the mechanical behaviour ofhealthy human descending thoracic aorta. Physiol Meas. 2010 Dec;31(12):1553-65. doi: 10.1088/0967-3334/31/12/001. PMID: 20980717.

33. Atienza JM, Guinea GV, Rojo FJ , et al. The Influence of Pressure and Temperature on the Behavior of the Human Aorta and Carotid Arteries. Rev Esp Cardiol. 2007 Mar;60(3):259-67. Spanish. PMID: 17394871.

34. Canales, Claudio. Characterization of hyperelastic models with metaheuristic algorithms. University of Santiago of Chile. M. Sc. thesis; 2020. Spanish.

35. Back T, Hammel U, Schwefel H-P Evolutionary computation: comments on the history and current state. EEE Transactions on Evolutionary Computation. 1997 Apr:1(1):3-17. doi: 10.1109/4235.585888.

36. Helfenstein J, Jabareen M, Mazza E, et al. On non-physical response in models for fiber-reinforced hyperelastic materials. J Mech Behav Biomed Mater. 2011 Oct;4(7):1359-68. doi: 10.1016/j.jmbbm.2011.05.006. PMID: 21783146.

37. Duong MT, Nguyen NH, Staat M. Physical response of hyperelastic models for composite materials and soft tissues. Asia Pac. J. Comput. Engin. 2, 3 (2015). https://doi.org/10.1186/s40540-015-0015-x.

38. Mezura-Montes E, Coello Coello CA An empirical study about the usefulness of evolution strategies to solve constrained optimization problems. International Journal of General Systems. 2008 Nov;37(4):443-473. https://doi.org/10.1080/03081070701303470

39. Holzapfel GA, Ogden RW. Constitutive modelling of arteries. Proc. R. Soc. A. 2010 Mar;466:1551–1597 https://doi.org/10.1098/rspa.2010.0058

40. Yang JM, Chen YP, Horng JT, Kao CY Applying family competition to evolution strategies for constrained optimization. International conference on evolutionary programming. Springer; 1997.

41. Demetrio M, Alexandre V, Dominique B. Application of evolution strategies for the solution of an inverse problem in near-field optics. J Opt Soc Am A Opt Image Sci Vis. 2004 Aug;21(8):1465-71. doi: 10.1364/josaa.21.001465. PMID: 15330475.

42. Beyer, Hans-Georg. The theory of evolution strategies. Springer Science & Business Media; 2001.

43. Ogden RW. Nonlinear elasticity with application to material modelling. Centre of Excellence for Advanced Materials and Structures; 2003.

44. Macrae RA, Miller K, Doyle BJ. Methods in Mechanical Testing of Arterial Tissue: A Review. Strain. 2016 May;52(5):380-399. J Opt Soc Am A Opt Image Sci Vis. 2004 Aug;21(8):1465-71. doi: 10.1364/josaa.21.001465. https://doi.org/10.1111/str.12183

45. M. Sasso and G. Palmieri and G. Chiappini and D. Amodio. Characterization of hyperelastic rubber-like materials by biaxial and uniaxial stretching tests based on optical methods. Polymer Testing 2008;27:995 - 1004 https://doi.org/10.1016/j.polymertesting.2008.09.001

46. Avril, Stéphane and Badel, Pierre and Duprey, Ambroise. Anisotropic and hyperelastic identification of in vitro human arteries from full-field optical measurements. J Biomech. 2010 Nov 16;43(15):2978-85 https://doi.org/10.1016/j.jbiomech.2010.07.004

47. Katia Genovese and Luciano Lamberti and Carmine Pappalettere Mechanical characterization of hyperelastic materials with fringe projection and optimization techniques. Optics and Lasers in Engineering. 44. 423-442. https://doi.org/10.1016/j.optlaseng.2005.06.003.

48. Rahnamayan, Shahryar and Tizhoosh, Hamid R and Salama, Magdy MA. A novel population initialization method for accelerating evolutionary algorithms. Computers & Mathematics with Applications. 53. 1605-1614. https://doi.org/10.1016/j.camwa.2006.07.013.

49. Moré, Jorge J. The Levenberg-Marquardt algorithm: implementation and theory. Numerical analysis; 1978.

50. Bozorg-Haddad, Omid and Solgi, Mohammad and Loáiciga, Hugo A Meta-heuristic and Evolutionary Algorithms for Engineering Optimization. John Wiley & Sons; 2017.

51. Back, Thomas. Evolutionary algorithms in theory and practice: evolution strategies, evolutionary programming, genetic algorithms; 2017. Oxford university press & Sons; 1996.

52. Bansal, Jagdish Chand and Singh, Pramod Kumar and Pal, Nikhil R. Evolutionary and swarm intelligence algorithms; 2019. Springer; 2019.